Nanoscale Horizons



COMMUNICATION

View Article Online



Cite this: Nanoscale Horiz., 2025, 10, 1096

Received 1st March 2025, Accepted 14th April 2025

DOI: 10.1039/d5nh00120j rsc.li/nanoscale-horizons

CoWO₄ nanoparticles with dual active sites for highly efficient ammonia synthesis†

Lian Duan,‡a Zhencong Huang,‡a Gen Chen,a Min Liu, b Xiaohe Liu,c Renzhi Ma * and Ning Zhang * * and Ning Zhang * * and Ning Zhang * and Nin

The electrochemical reduction reaction of NO₃⁻ (NO₃RR) represents a promising green technology for ammonia (NH₃) synthesis. Among various electrocatalysts, Co-based materials have demonstrated considerable potential for the NO₃RR. However, the NH₃ production efficiency of Co-based materials is still limited due to challenges in the competitive hydrogen evolution reaction (HER) and hydrogenating oxynitride intermediates (*NO_x). In this study, tungsten (W) and cobalt (Co) elements are co-incorporated to form cobalt tungstate (CoWO₄) nanoparticles with

[†] Electronic supplementary information (ESI) available: Experimental section, supplementary figures and tables. See DOI: https://doi.org/10.1039/d5nh00120j ‡ These authors contributed equally to this work.



Renzhi Ma

Congratulations to Nanoscale Horizons for a decade of actively promoting high-level interdisciplinary research in nanoscience and nanotechnology! Our first paper was published in Nanoscale Horizons in 2019. We are proud to contribute this article and receive the honor to be featured in the 10th anniversary collection. As a board member of the Nanoscale journal family, we are keen to continue to report research advances the

exploration of novel nanomaterials toward the development of highperformance electrocatalysts for energy-related applications in this prominent journal. Best wishes to Nanoscale Horizons for another exciting decade.

New concepts

Tungsten and cobalt elements are co-incorporated to form cobalt tungstate (CoWO₄) nanoparticles, which feature bimetallic W and Co active sites. These nanoparticles are employed to optimize the hydrogenation of *NO_x and suppress hydrogen evolution reactions, thereby facilitating highly efficient NO3- reduction to NH3. Theoretical calculations reveal that Co sites in CoWO₄ promote the adsorption and hydrogenation of *NO_r intermediates, while W sites inhibit the competing hydrogen evolution reaction (HER). These dual active sites work synergistically to enhance NH3 production during NO3reduction. Guided by these computational insights, CoWO4 nanoparticles are synthesized via a simple ion precipitation method, with sizes ranging from 10 to 30 nm. Electrochemical testing demonstrates that CoWO4 nanoparticles achieve a high faradaic efficiency of 97.8 ± 1.5% and an NH3 yield of 13.2 mg h⁻¹ cm⁻², significantly outperforming the corresponding WO₃ and Co₃O₄ materials as well as most reported electrocatalysts. In situ Fourier transform infrared spectroscopy reveals the enhanced adsorption and hydrogenation of *NOx intermediates and the suppression of the HER on CoWO₄, which contributes to the high efficiency and selectivity toward NH₃. This study presents a simple yet effective strategy for the design and synthesis of electrocatalytic materials by precisely tailoring active sites with distinct functions, which advances the development of highly efficient electrocatalysts for NH₃ production.

dual active sites of Co²⁺ and W⁶⁺, which are applied to optimize the hydrogenation of NO_x and decrease the HER, thereby achieving a highly efficient NO₃RR to NH₃. Theoretical calculations indicate that the Co sites in CoWO₄ facilitate the adsorption and hydrogenation of *NO_x intermediates, while W sites suppress the competitive HER. These dual active sites work synergistically to enhance NH₃ production from the NO₃RR. Inspired by these calculations, CoWO₄ nanoparticles are synthesized using a simple ion precipitation method, with sizes ranging from 10 to 30 nm. Electrochemical performance tests demonstrate that CoWO₄ nanoparticles exhibit a high faradaic efficiency of 97.8 \pm 1.5% and an NH $_3$ yield of 13.2 mg h⁻¹ cm⁻². In situ Fourier transform infrared spectroscopy characterizes the enhanced adsorption and hydrogenation behaviors of *NO_x as well as a minimized HER on CoWO₄, which contributes to the high efficiency and selectivity to NH₃. This work introduces CoWO₄ nanoparticles as an electrocatalytic material with dual active sites, contributing to the design of electrocatalysts for NH₃ synthesis.

^a School of Materials Science and Engineering, Central South University, Changsha, 410083, China, E-mail: nzhang@csu.edu.cn

^b School of Physics and Electronics, Central South University, Changsha, 410083, China

^c School of Chemical Engineering, Zhengzhou University, Zhengzhou, 450001, China

^d Research Center for Materials Nanoarchitectonics (MANA), National Institute for Materials Science (NIMS), Tsukuba, Ibaraki, 305-0044, Japan. E-mail: ma.renzhi@nims.go.jp

1. Introduction

Communication

Ammonia (NH₃) is essential for producing fertilizers and nitrogen compounds, largely via the Haber-Bosch process, which synthesizes NH₃ from N₂ and H₂. Due to the high energy required to break the N≡N bond (941 kJ mol⁻¹), this process requires extreme temperatures (400-600 °C) and pressures (200-300 atm).^{2,3} The required H₂ comes from methane steam reforming, generating substantial CO2 emissions, contributing to environmental concerns. 4,5 Electrocatalytic synthesis offers an ecofriendly, energy-efficient method for NH₃ production using renewable resources. 6-8 While the nitrogen reduction reaction (NRR) is promising, challenges such as the hydrogen evolution reaction (HER), low N2 solubility, and the high dissociation energy of the N=N bond limit faradaic efficiency and NH₃ yield. 9,10 Using nitrate (NO₃⁻) instead of N₂ improves water solubility and reduces the energy required for bond dissociation, making it an ideal nitrogen source. 11-13 Moreover, the NO₃ reduction reaction (NO₃RR) can convert wastewater pollutants into NH₃, offering a strategy to balance the nitrogen cycle. 14-16 However, the NO₃RR is a complex, slow process requiring eight-electron transfer, and it generates by-products like NO₂⁻, N₂, and H₂. ^{17,18} Effective hydrogenation of adsorbed oxynitride intermediates (*NO_x, e.g., *NO₃ and *NO2) and suppressed HER during the catalytic process are important to enhance the formation of NH₃. ^{19,20}

Transition metal-based oxide electrocatalytic materials, such as NiO, Co₃O₄, Fe₂O₃, and MnO₂, have been demonstrated to exhibit high hydrolysis dissociation activity and distinct electrocatalytic activity for the HER or oxygen evolution reaction (OER).21-24 In the context of the NO₃RR, their remarkable hydrolysis dissociation capability provides substantial quantities of *H for the hydrogenation of NO_x intermediates. Among them, Co based materials are promising electrocatalysts due to the strong electrostatic interaction of Co 3d electrons with NO₃ as well as strong hydrolysis dissociation capability to provide *H for hydrogenation of NO_x intermediates.^{25,26} For example, Zhang et al. reported electron-deficient Co metal nanocrystals for improving both NO3 adsorption and *NH hydrogenation to enhance the NH₃ production in the NO₃RR.²⁷ Gu et al. designed ultrathin CoO_r nanosheets with abundant adsorbed oxygen species, which hampers the HER on cobalt oxide and leads to an enhanced NO₃RR activity.²⁸ Lu et al. synthesized a Co₃O₄ nanosheet array with cobalt vacancies on carbon cloth, which exhibited a high faradaic efficiency.²⁹ However, competitive HER generally occurs intensively on most Co based materials within aqueous electroreduction systems, which hinders the selectivity of the NO₃RR and causes a decrease of NH₃ production efficiency.

On the other hand, tungsten (W) based oxide materials such as WO3 are regarded as a prospective electrocatalyst for the NO₃RR due to its low cost, strong electronegativity, and excellent electrochemical stability. 30,31 Prior research indicates that the 5d electron orbital of W exhibited an exceptionally robust adsorption capacity for reactive hydrogen, impeding the desorption of *H and contributing to the suboptimal HER.³² From the perspective of electrocatalytic NO₃RR, a stronger *H

adsorption capacity and low tendency for the HER are favourable for achieving efficient NH3 production. 33,34 However, for pristine WO3 materials, the too sluggish HER resulting from strong *H adsorption introduces a high energy barrier for hydrogenation of *NOx, thereby restricting its involvement in the hydrogenation process and causing the excessive formation of NO2-. Therefore, it is essential to maintain a balanced state for NO_r hydrogenation and the HER.

In this work, tungsten oxides and cobalt oxides are coincorporated to form cobalt tungstate (CoWO₄) with bimetallic Co-W dual active sites to optimize the hydrogenation of *NO_x intermediates and decrease the HER process to enhance the electrochemical NO₃RR to NH₃. Density functional theory (DFT) calculations predict that Co sites in CoWO4 benefit the adsorption and hydrogenation of NO_x intermediates, while W sites decrease water dissociation and the HER, which exhibits a synergistic high efficiency in electrocatalytic reduction of NO₃ to NH₃. Inspired by DFT calculations, the CoWO₄ nanoparticles are synthesized via a one-step precipitation method. CoWO₄ exhibits excellent NO₃RR performance across a broad potential range, spanning from -0.2 to -0.7 V versus the reversible hydrogen electrode (vs. RHE). At a potential of -0.4 V, the maximum Faraday efficiency (FE) of NH3 generation on CoWO4 is 97.8 \pm 1.5%, which is significantly higher than that of WO₃ $(60.1 \pm 5.8\%)$ and $\mathrm{Co_3O_4}$ $(83.9 \pm 5.1\%)$. In situ Fourier-transform infrared (FT-IR) spectroscopy further confirms that CoWO₄ not only enhances the hydrogenation of *NOx intermediates but also minimizes the HER, thus facilitating efficient NO₃RR to produce NH₃. This work offers an effective strategy to engineer high performance NO₃RR electrocatalysts based on bimetallic oxides.

Experimental

2.1 Synthesis of CoWO₄ nanoparticles

CoWO₄ nanoparticles were synthesized by an ion precipitation method. In a typical procedure, 1.455 g of Co(NO₃)₂·6H₂O (5 mmol) and 1.649 g of Na₂WO₄·2H₂O (5 mmol) were added into 60 mL deionized water. Then, the solution was mixed and heated to 70 °C for 3 hours with constant stirring. The resulting suspension and precipitate were subjected to washing with deionized water and ethanol, followed by several rounds of centrifugation. Finally, the CoWO₄ powder was obtained through oven drying.

2.2 Synthesis of WO₃ and Co₃O₄ nanoparticles

In the preparation of Co₃O₄ nanoparticles, 20 mL of 0.5 M Na₂CO₃ was added dropwise to the solution of Co(NO₃)₂·6H₂O (0.291 g dissolved in 20 mL deionized water) under constant stirring. In order to synthesize WO3 nanoparticles, 20 mL of 0.1 M HCl was added dropwise to a solution of sodium tungstate (0.329 g dissolved in 20 mL deionized water) under constant stirring. Subsequently, the mixed solution was subjected to a series of washes with deionized water and ethanol, followed by several rounds of centrifugation. The precipitate obtained following drying was subjected to calcination in a muffle furnace at 500 °C in air for a period of two hours,

Nanoscale Horizons Communication

resulting in the formation of Co₃O₄ and WO₃ nanoparticles, respectively.

Details on the electrocatalytic performance tests, DFT computations, characterizations, $\mathrm{NH_3}$ and $\mathrm{NO_2}^-$ quantification, faradaic efficiency and yield rate calculations, and *in situ* measurements are described in the ESI.†

3. Results and discussion

3.1 Theoretical calculations

DFT calculations were initially employed to investigate the adsorption properties of *NO_x intermediates and *H₂O species over the surface of WO₃, Co₃O₄, and CoWO₄. The (001) surfaces of WO₃, Co₃O₄, and CoWO₄ were constructed for calculations (Fig. 1a), and additional DFT computational details could be found in the ESI.† As illustrated in Fig. 1b, the adsorption energies of *NO₃ and *NO2 on WO3, CO3O4, and CoWO4 surfaces were initially investigated. From the calculated values in Fig. 1c, it can be observed that the adsorption energies of *NO3 on the surfaces of the catalysts are 0.55, -0.75, and -0.86 eV for WO₃, CoWO₄, and Co₃O₄, respectively. And we also investigated the adsorption energies of *NO3 on the Co and W sites of CoWO4 and electron transfer between active sites and NO₃⁻ (Fig. S1, ESI†). The adsorption of *NO3 is more favourable at the Co sites than at the W sites, suggesting that the NO₃RR is more likely to occur at the Co sites. And the adsorption energies of *NO2 on the surfaces of catalysts are -0.45, -1.63, and -2.07 eV for WO₃, CoWO₄, and Co₃O₄, respectively. The *NO₂ is thus more easily adsorbed on Co₃O₄ and CoWO₄.

Subsequently, the Gibbs free energy for each reaction step on these catalyst surfaces was calculated to examine the effect of *NO_x adsorption on the reaction pathway of the NO₃RR (atomic models are shown in Fig. S2-S4, ESI†). We considered that the reaction pathways from NO_3^- to NH_3 are as follows: (*+ NO_3^-) \rightarrow *NO $_3$ \rightarrow *NO $_3$ H \rightarrow *NO $_2$ \rightarrow *NO $_2$ H \rightarrow *NO \rightarrow *NOH \rightarrow *N *NH \rightarrow *NH₂ \rightarrow *NH₃.³⁵ As presented in Fig. 1d, the results of the calculated Gibbs free energies demonstrate that the formation of *NO₃ intermediates on the CoWO₄ and Co₃O₄ surfaces exhibits a negative free energy, indicating that CoWO₄ and Co₃O₄ have a strong adsorption capacity for NO₃⁻. Furthermore, the maximum reaction Gibbs free energy change (ΔG_{max}) of the NO₃RR on WO₃, CoWO₄, and Co₃O₄ occurs in the step of *NO₂ to *NO₂H, suggesting that the hydrogenation of *NO₂ is the ratedetermining step (RDS) of the reaction. Fig. 1e illustrates the ΔG_{max} of the hydrogenation of *NO₂ to *NO₂H on WO₃, Co₃O₄ and CoWO₄, which are 1.64, 1.42 and 1.04 eV, respectively. It is evident that the CoWO₄ lowers the reaction energy barrier of the RDS, which is favourable to the *NO₂ hydrogenation process.

The H_2O dissociation process on WO_3 , Co_3O_4 , and $CoWO_4$ is also investigated (Fig. S5–S8, ESI†). Fig. S5 (ESI†) shows that the stronger adsorption of *H and H_2O occurs more easily on the W sites than on the Co sites in $CoWO_4$, indicating that the hydrolysis process occurs predominantly on the W sites. The calculation results of the H_2O dissociation process in Fig. 1f demonstrate that the hydrolysis barrier on $CoWO_4$ is lower than

that on WO₃, but higher than that on CO₃O₄. Furthermore, the HER process on the catalyst is also investigated (Fig. S9, ESI†). The results demonstrate that CO₃O₄ has notable activity for the HER, while the HER process on WO₃ and CoWO₄ is relatively slow (Fig. 1g). The above DFT calculations indicate that the CoWO₄ material exhibits favourable adsorption of *NO₂ and an efficient RDS for the conversion of *NO₂ to *NO₂H in comparison with WO₃ and Co₃O₄. Additionally, it possesses a relatively minimized hydrolysis and HER process, which together make CoWO₄ have a potentially exceptional ability to reduce NO₃ $^-$ to NH₃.

3.2 Characterization analysis

Inspired by the theoretical calculations, we synthesized CoWO₄ nanoparticles using Na₂WO₄·2H₂O and Co(NO₃)₂·6H₂O as raw materials through a straightforward one-step precipitation method, followed by drying at 60 °C (Fig. S10, ESI†). Fig. 2a presents the X-ray diffraction (XRD) pattern of the synthesized WO₃, Co₃O₄, and CoWO₄. The XRD pattern indicates that the diffraction peaks of the prepared CoWO4 correspond well with monoclinic CoWO₄ (JCPDS No. 15-0867), confirming the successful synthesis of monoclinic-phase CoWO₄ with a P2/a space group. And the XRD patterns of the synthesized pure WO₃ and Co₃O₄ correspond well with monoclinic WO₃ (JCPDS No. 71-2141) and cubic Co₃O₄ (JCPDS No. 73-1701), respectively. The morphologies of the above synthesized catalysts were characterized by scanning electron microscopy (SEM), transmission electron microscopy (TEM), and high-resolution TEM (HR-TEM). CoWO₄ exhibits a particle morphology (Fig. 2b and c), which are in an aggregated state of irregular nanoparticles with a size of about 20-30 nm. And CoWO4 has a more uniform and smaller nanoparticle morphology. Fig. 2d and Fig. S11 (ESI†) show the TEM images of CoWO₄, revealing that the nanoparticles are approximately 20 nm in size and exhibit an irregular shape. The HR-TEM image of CoWO₄ in Fig. 2e shows a crystalline region with an interplanar spacing of 0.46 nm, corresponding to the (001) plane of monoclinic CoWO₄. Additionally, Fig. 2f presents the high-angle annular dark-field scanning transmission electron microscopy (HAADF-STEM) images of CoWO4 along with the corresponding energydispersive X-ray spectroscopy (EDS) elemental mapping images, illustrating the uniform distribution of W, Co, and O elements throughout the CoWO₄ nanoparticles. Fig. 2g illustrates the microscopic atomic structure model of CoWO₄, wherein alternating Co and W are discernible. To clarify the physical nature of the prepared CoWO4 catalyst, we conducted the IR and Raman characterization of the catalysts. According to the IR and Raman profiles, the as-prepared CoWO4 is monophasic (Fig. S12, ESI†). The SEM images of WO₃ in Fig. 2h and Fig. S13 (ESI†) show that WO₃ displays a significantly larger irregular nanoparticle morphology, with sizes around 200-300 nm. TEM images of WO₃ (Fig. 2i and Fig. S14, ESI†) reveal that the nanoparticles are larger, with sizes around 200-300 nm, consistent with the SEM results. The HR-TEM image in Fig. S14 (ESI†) demonstrates that the entire WO₃ lattice exhibits a highly ordered rectangular array, characterized by alternating atomic arrangements. The further magnified HR-TEM image shows

Communication Nanoscale Horizons

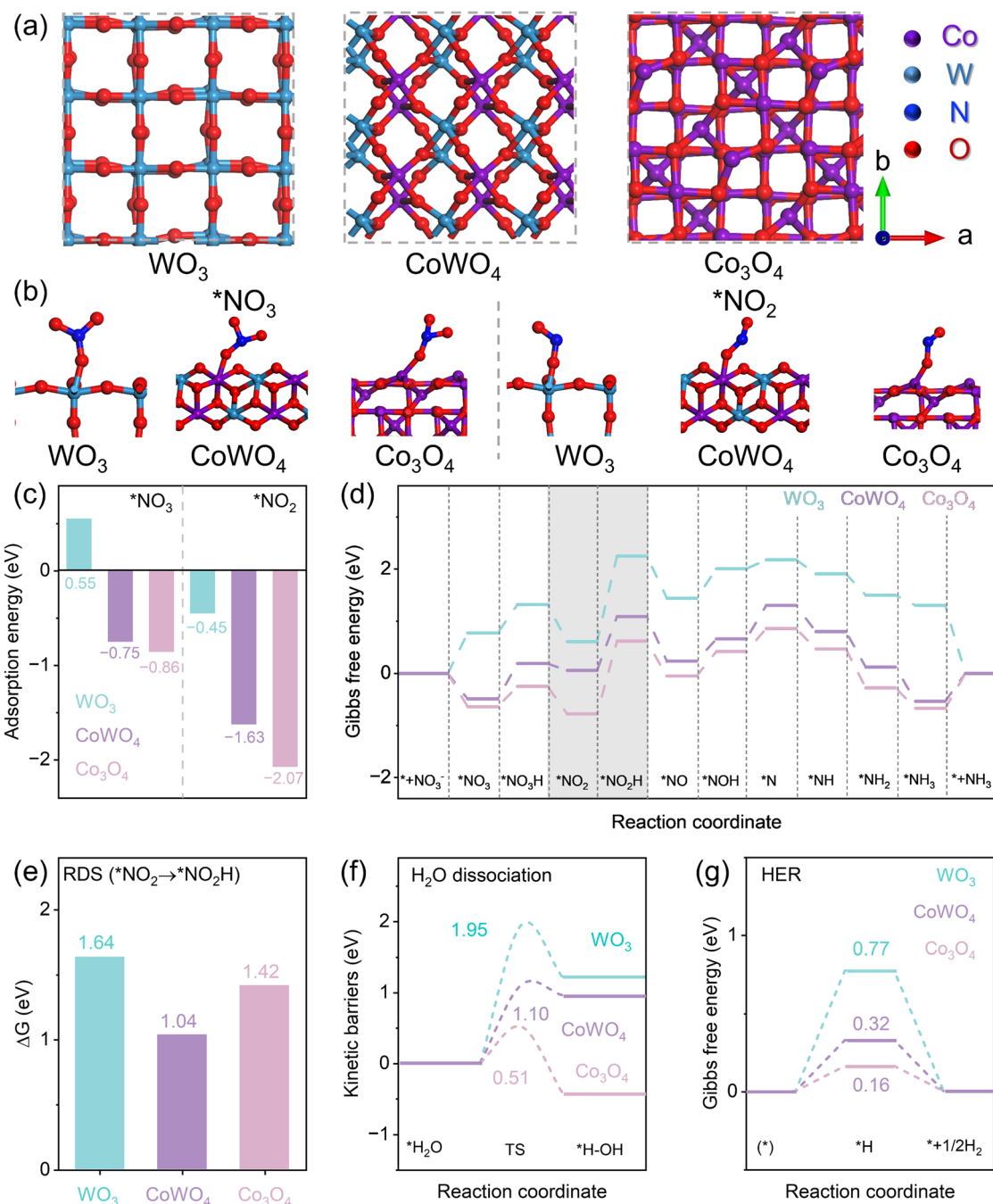


Fig. 1 (a) The atomic models of the (001) surface for WO₃, CoWO₄, and Co₃O₄. (b) The adsorption configurations of *NO₃ and *NO₂ intermediates on WO₃, $CoWO_4$, and Co_3O_4 surfaces. (c) The adsorption energies of * NO_3 and * NO_2 intermediates. (d) Reaction Gibbs free energies for different reaction intermediates and (e) the reaction Gibbs free energy changes (ΔG) of the RDS on the W site of WO₃, the Co site of CoWO₄, and the Co site of Co₃O₄. (f) Energy barrier of the H₂O dissociation process and (g) the reaction Gibbs free energy of the HER on the W site of WO₃, the W site of CoWO₄, and the Co site of Co₃O₄.

that the atomic spacing in the transverse and longitudinal directions is 0.38 nm and 0.37 nm, respectively, corresponding to the (002) and (020) planes of monoclinic WO₃. In contrast, Fig. 2j and Fig. S13 (ESI†) show that Co₃O₄ appears as agglomerated nanoparticles with sizes ranging from about 30 to 60 nm. The TEM images of Co₃O₄ display a relatively uniform nanoparticle morphology with an average size of approximately 40 nm (Fig. 2k and Fig. S14, ESI†). Fig. S14 (ESI†) reveals that

Co₃O₄ has good crystallinity, and the further magnified HR-TEM image shows an interplanar spacing of 0.24 nm, corresponding to the (311) plane of cubic Co₃O₄. The aforementioned study validates the successful synthesis of CoWO4, WO3, and Co₃O₄ nanoparticles.

In order to further understand the composition of the catalyst, X-ray photoelectron spectroscopy (XPS) and X-ray absorption fine structure spectroscopy (XAFS) were used to

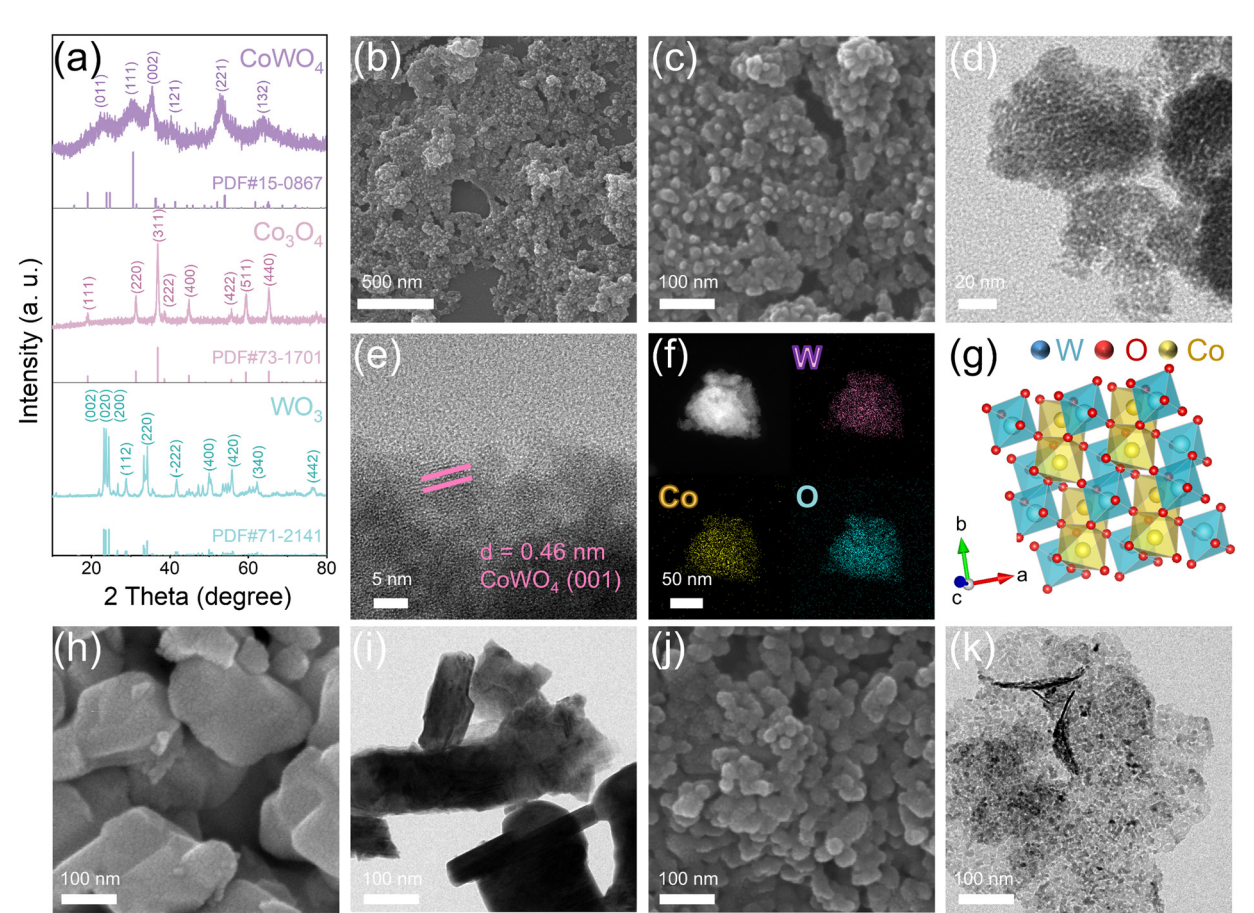


Fig. 2 (a) XRD patterns of CoWO₄, Co₃O₄, and WO₃; (b) and (c) SEM images of CoWO₄; (d) TEM image of CoWO₄; (e) HR-TEM image of CoWO₄; (f) HAADF-STEM image of CoWO₄ and the corresponding EDS elemental maps of W, Co, and O; (g) microscopic atomic structure modeling of CoWO₄; (h) and (i) SEM and TEM images of WO3; (j) and (k) SEM and TEM images of Co3O4.

analyze the surface chemistry and valence state of the materials. All XPS spectra were calibrated by the C 1s peak of adventitious carbon at 284.8 eV. Fig. S15 (ESI†) shows the full XPS spectra of CoWO₄, WO₃, and Co₃O₄. The XPS full spectrum of CoWO₄ reveals the presence of characteristic peaks corresponding to the W, Co, O, and C elements. The carbon comes from the environments during the measurements. The absence of additional impurity peaks suggests that no additional impurity elements were introduced into the prepared samples. Fig. 3a-c show the high-resolution XPS spectra of W 4f, Co 2p and O 1s for CoWO₄, respectively. As shown in Fig. 3a, the XPS spectrum of W 4f shows two different split spin-orbit peaks, located at 35.2 and 37.4 eV, which correspond to a pair of typical characteristic peaks of W-O bonds (W⁶⁺ $4f_{7/2}$ and W⁶⁺ $4f_{5/2}$). 36,37 The XPS spectrum of Co 2p in Fig. 3b can be divided into spin-orbit peaks and satellite peaks, and the spin-orbit peaks can be divided into Co $2p_{3/2}$ and Co $2p_{1/2}$ regions; among them, the pair of peaks at 782.5 and 798.2 eV correspond to Co²⁺, while the pair of peaks at 780.6 and 796.8 eV correspond to Co³⁺, which is consistent with the reports in the literature.³⁸ Additionally, the two peaks at 787.1 and 803.3 eV are the satellite peaks of Co 2p. 39 In the highresolution XPS spectrum of O 1s, as shown in Fig. 3c, the O 1s spectrum can be divided into three sub-peaks at 530.3, 531.4,

and 532.9 eV, corresponding to lattice oxygen (OL, M-O bond), defect oxygen (OD) and adsorbed oxygen (OA), respectively. 39,40 The corresponding Fourier transform magnitudes in the *R* space of the W L₃-edge demonstrates the presence of W-O bonds in WO₃ and CoWO₄ (Fig. 3d).⁴¹ In addition, the high-resolution XPS spectra of WO₃ and Co₃O₄ are also characterized, which are consistent with the typical WO₃ and Co₃O₄ materials (Fig. S16, ESI†).42-45 The above results prove the successful synthesis of CoWO₄, WO₃, and Co₃O₄.

3.3 Catalytic performance analysis

Subsequently, the electrochemical NO₃RR performance of the synthesized catalysts was investigated in an alkaline electrolyte (1 M NaOH + 0.1 M NaNO₃) using a typical H-type electrolytic cell. The linear sweep voltammetry (LSV) curves of the catalysts were recorded under controlled conditions. As shown in Fig. 4a, the addition of NO₃⁻ to the electrolyte led to a significant increase in current density in all three catalysts, indicating that NO₃⁻ actively participated in the reduction reaction, and the NO₃RR occurred in the solution system. CoWO₄ exhibits the highest current density compared to WO3 and CO3O4. Additionally, CoWO4 shows a significant increase in current density compared to the electrolyte without NO₃⁻ (Fig. S17, ESI†), indicating its superior catalytic

Communication Nanoscale Horizons

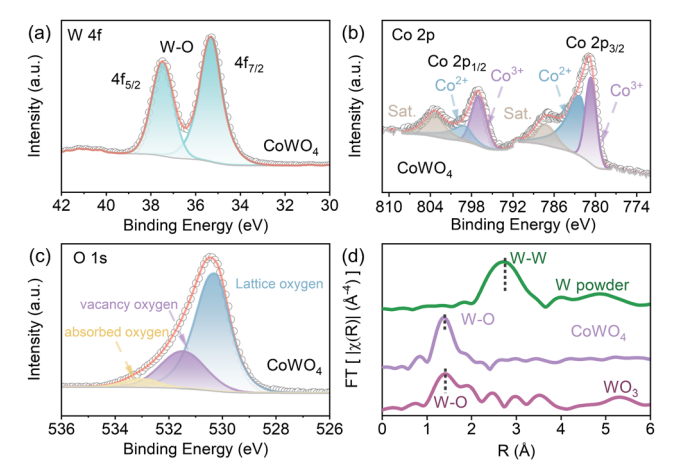


Fig. 3 High resolution XPS spectra of (a) W 4f, (b) Co 2p, and (c) O 1s for CoWO₄. (d) Fourier transform magnitudes in R space of the W L₃-edge for WO3, CoWO4, and W powder.

activity for the NO₃RR. And the Tafel slopes are fitted according to the LSV curves during the NO₃RR process (Fig. 4b). CoWO₄ has the lowest Tafel slope (310.9 mV dec⁻¹) during the NO₃RR, which is much lower than those of WO₃ (443.1 mV dec⁻¹) and Co₃O₄ (345.1 mV dec⁻¹), suggesting that the CoWO₄ surface has faster NO₃RR kinetics.

Then, we investigated the selectivity of electrochemical NO₃RR at different potentials. The concentrations of NH₃ and NO2 in the electrolyte were detected by indoxyl blue colorimetry (Fig. S18, ESI†). The faradaic efficiencies of NH3 at varying potentials were determined through chronoamperometry and UV-visible absorbance measurements (Fig. S19, ESI†). According to the LSV curves of the catalysts, a suitable voltage range (-0.2 to -0.7 V vs. RHE) was selected to perform chronoamperometric (CA) electrolysis tests on the catalysts to more comprehensively evaluate the NO₃RR performance of the catalysts. Fig. S19a-c (ESI†) show the CA curves of CoWO₄, WO₃, and Co₃O₄ at different potentials. It can be seen that the current of the electrolysis reaction improves with the increase of the applied voltage. CoWO4 shows the highest reaction current at each applied voltage, indicating that it has a relatively superior NO₃RR activity to WO₃ and Co₃O₄. After the electrolysis experiment, the electrolyte in the cathode chamber

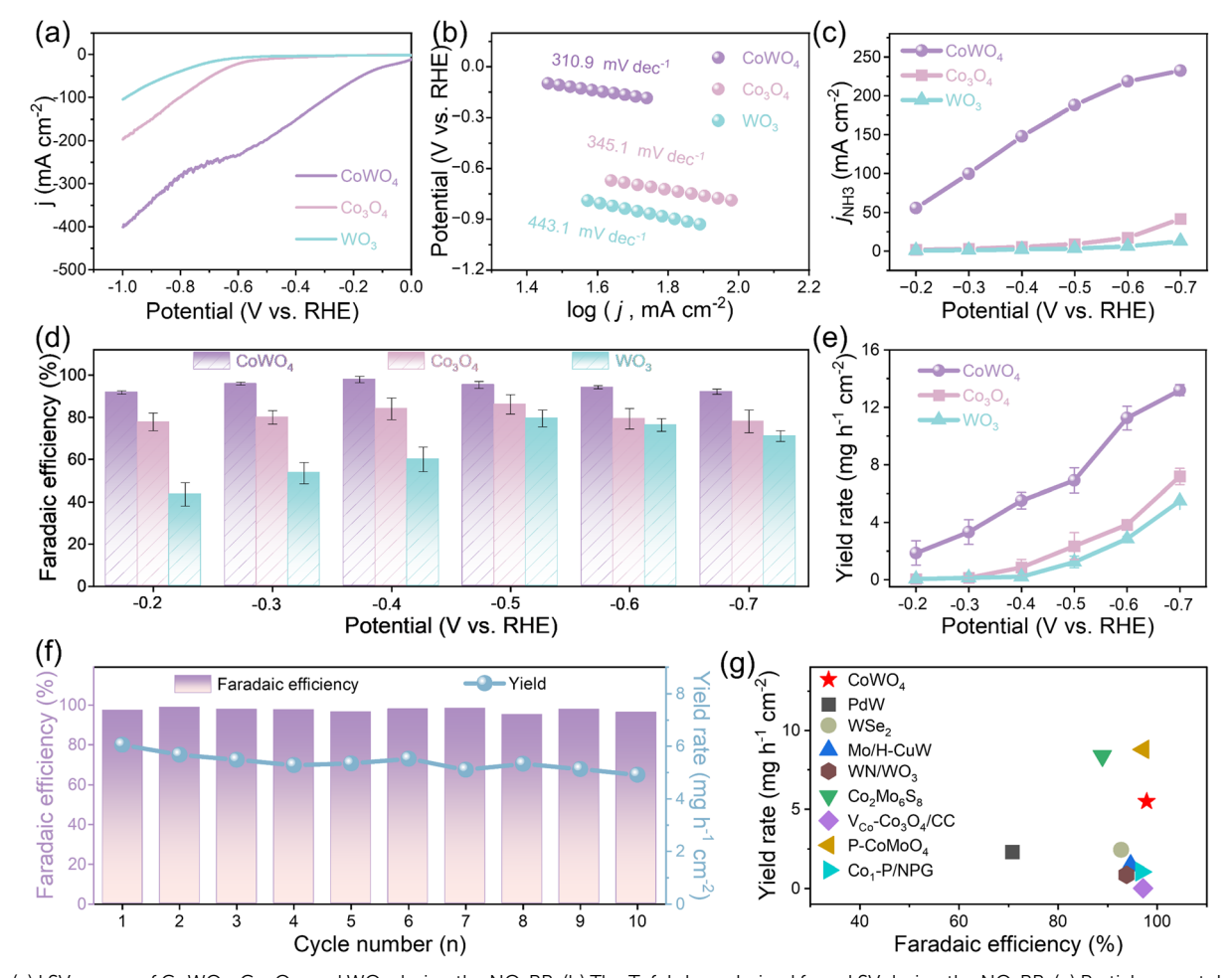


Fig. 4 (a) LSV curves of CoWO₄, Co₃O₄, and WO₃ during the NO₃RR. (b) The Tafel slope derived from LSV during the NO₃RR. (c) Partial current density of NH₃ production under different potentials. (d) Faraday efficiencies of NH₃ production under different potentials. (e) Yield rate of NH₃ at different potentials. (f) FE and NH₃ yields during the cycling stability test. (g) The comparison of CoWO₄ with other reported catalysts.

Nanoscale Horizons Communication

of the electrolytic cell was collected and diluted to an appropriate concentration to determine the NH3 content by the indophenol blue method. Fig. S19d-f (ESI†) shows the UVvisible absorption spectra of CoWO₄, WO₃ and Co₃O₄, respectively. The FE_{NH_2} can be calculated using the reaction current and the corresponding absorbance. The partial current density, FEs and yield rates of NH3 under different potentials are also shown in Fig. 4c-e. It shows that the partial current density (j_{NH_2}) of CoWO₄ for NH₃ generation is significantly better than that of WO₃ and Co₃O₄. In addition, Fig. 4d illustrates the FE of the catalyst for NH₃ generation at various potentials. It can be seen that, with the increase of the applied potential, the FE firstly increases and then decreases, and the FE of all catalysts shows a volcano diagram trend. CoWO4 shows superior selectivity and FE_{NH}, at all potentials compared to WO₃ and Co₃O₄. The FE at all test potentials exceeds 91.7% for CoWO₄, which is much higher than those of WO₃ and Co₃O₄. Among them, at a potential of -0.4 V vs. RHE, the maximum FE of NH₃ generation on CoWO₄ can reach 97.8 \pm 1.5%, which is much higher than those on WO₃ (60.1 \pm 5.8%) and Co₃O₄ (83.9 \pm 5.1%). Based on the high selectivity and current density for NH₃ generation, CoWO₄ can also show a significantly higher NH₃ yield, where the yield is 5.5 ± 0.6 mg h^{-1} cm $^{-2}$ at -0.4 V. The maximum NH₃ yield reaches 13.2 mg h⁻¹ cm⁻² at -0.7 V and the FE is 92.1% at this time, which is much higher than those of WO₃ (5.4 mg h⁻¹ cm⁻²) and Co₃O₄ (7.1 mg h⁻¹ cm⁻²). The above results suggest that CoWO4 has obviously enhanced NO₃RR performance than WO₃ and Co₃O₄. To double check the production of NH3 from CoWO4, Nessler's test was employed to determine the production rate of NH₃. The comparable results obtained using Nessler's reagent are shown in Fig. S20 (ESI†), confirming the great reliability of the detection results of the indophenol blue method.

The NO₃RR performances of CoWO₄ in low-concentration NO₃⁻ (100, 50, 20, and 10 mM) electrolytes were also studied. Fig. S21a (ESI†) shows the LSV curves obtained in electrolytes with different NO₃⁻ concentrations. As the NO₃⁻ concentration in the electrolyte decreases, the current response of the LSV obtained also gradually decreases, showing that the NO₃RR activity decreases accordingly. Subsequently, their NO₃RR selectivity and efficiency were studied at a voltage of -0.4 V. Fig. S21b and c (ESI†) show the corresponding chronoamperometric curves and UV curves of the solution after the reaction. The *i-t* curve during the reaction also shows a gradually decreasing trend with decreasing NO₃⁻ concentration. As shown in Fig. S21d (ESI†), CoWO₄ can exhibit FE_{NH}, values of 97.9%, 94.8% and 91.8% under the electrolysis conditions of 100 mM, 50 mM and 20 mM NO₃ concentrations, respectively. Even in the electrolyte with an extremely low NO₃⁻ concentration (10 mM), its FE of the NO₃RR to synthesize NH₃ is 83.4%. So, CoWO₄ has relatively excellent NO₃RR activity under low NO₃ concentration electrolyte conditions. The as-prepared CoWO₄ materials have potential application prospects in electrocatalytic synthesis of NH₃ from wastewater.

In order to exclude the interference of other nitrogen sources that may exist in the experiment and ensure that the NH₃ produced in the experiment comes from NO₃⁻ in the electrolyte rather than other pollutants, a blank control experiment without NO₃⁻ electrolyte and without applied voltage was carried out. Fig. S22 (ESI†) shows the UV curves obtained by detecting the electrolyte under a series of different experimental conditions. Obviously, under the conditions of electrolyte without NO₃ and electrolyte with NO₃ without applied voltage, obvious adsorption peaks are difficult to detect in the UV curve, indicating that there is no NH₃ produced in the electrolyte. The results show that negligible amounts of NH3 are detected in the absence of NO₃ or without applying a voltage. However, when NO₃⁻ is present and a voltage is applied, a significant NH3 yield and FE are achieved. The above results indicate that there is no contamination from any other nitrogen source during the experiment, ensuring that the NH3 in the solution is produced from electrolytic reduction of NO₃⁻ in the electrolyte.

To assess the stability of the CoWO₄ catalyst, both cyclic electrolysis and long-term continuous electrolysis tests were carried out at a potential of -0.4 V. During the cyclic electrolysis test, the electrolyte was collected every 30 minutes for colorimetric analysis. After each cycle, the electrolytic cell was cleaned, and the electrolyte was replaced before the next cycle. The chronoamperometric curves for each cycle and the corresponding UV spectra of the electrolyte are shown in Fig. S23 (ESI†). A slight decrease in current density is observed after the first cycle, but the electrolysis current remained stable in subsequent cycles. No significant decrease is detected during the cyclic test, and the corresponding UV spectra show minimal variation. As shown in Fig. 4f, after 10 cycles, the FE and NH₃ yield of CoWO₄ remain stable, with the FE exceeding 96% and the NH₃ yield maintained at approximately 5.5 mg h⁻¹ cm⁻², indicating excellent stability. Additionally, a 21-hour continuous electrolysis test was performed (Fig. S24, ESI†), without replacing the electrolyte or electrodes. The electrolyte was periodically collected for colorimetric analysis, and its UV spectra were recorded (Fig. S25, ESI†). The *i-t* curve in Fig. S23 (ESI†) shows stable current throughout the electrolysis, with no significant fluctuations in current density. The corresponding FE of NH₃ remains consistent throughout the test. After 21 hours, the FE is still above 88.9%. The slight decline in FE may be due to the gradual depletion of NO₃ in the electrolyte over time. These results demonstrate the excellent electrocatalytic stability of CoWO₄ for the NO₃RR. Furthermore, ITO conductive glass was employed as the substrate for catalyst loading to test the XRD patterns of the catalyst before and after the electrochemical reaction (Fig. S26, ESI†). The results reveal that there is no shift in peak positions or the appearance of new peaks after the reaction, except for a reduction in the intensity of the CoWO₄ diffraction signal, which is likely due to catalyst detachment from the ITO substrate during the electrochemical test. The structural characterizations and the corresponding EDS elemental maps of CoWO₄ after reduction are shown in Fig. S27 and S28 (ESI†). The above results suggest that CoWO4 exhibits excellent durability and stability for the NO₃RR to produce NH₃. Furthermore, the electrocatalytic performance of CoWO4 is benchmarked against other

Communication Nanoscale Horizons

previously reported catalysts (Fig. 4g and Table S1, ESI†), revealing that CoWO4 nanoparticles exhibit a relatively superior FE and excellent NH3 yield, outperforming most reported Co- and Wbased catalysts. 19,29,46-51

In addition, the FEs of the byproducts (such as NO₂⁻, N₂ and H₂) that may appear during the NO₃RR are also calculated. It can be seen that NH3 and NO2 are the main nitrogencontaining products. Fig. S29a-c (ESI†) show the corresponding UV curves for the detected NO₂⁻. According to the gas chromatograph detection results in Fig. S28d-f (ESI†), there is no N₂ detected during the reaction, and only a small amount of H₂ is detected. Fig. 5a-c show the main products of the NO₃RR of CoWO₄, Co₃O₄ and WO₃, respectively. As the applied voltage increases, NO₂ is gradually converted and consumed, and the HER becomes increasingly intense. It is clearly seen that CoWO₄ generates fewer by-products of NO₂⁻ than WO₃ and Co₃O₄, which is attributed to its more favorable hydrogenation ability as predicted by DFT calculations. Meanwhile, the HER process in CoWO4 is obviously decreased in comparison with WO₃ and Co₃O₄, which is well consistent with the DFT calculation results. Therefore, in comparison to WO₃ and Co₃O₄, CoWO₄ demonstrates a decreased HER process and a high NO_x hydrogenation ability, which together contribute to its superior capability to reduce NO₃⁻ to NH₃.

To deeply evaluate the intrinsic activity of these catalysts, kinetic electrochemical impedance spectroscopy (EIS) and electrochemically active surface area (ECSA) tests were conducted. Fig. 5d shows the fitted EIS of CoWO₄, Co₃O₄, and WO₃. The inset in the figure shows the fitting model, which includes the charge transfer resistance (R_{ct}), solution resistance (R_{s}) and a constant phase element (CPE). From the further enlarged EIS

graph, it can be seen that the R_s values of the three catalysts are very close. CoWO4 has a significantly smaller charge transfer impedance (7.91 Ω). So, compared with WO₃ (303.80 Ω) and Co_3O_4 (194.00 Ω), $CoWO_4$ has a higher mass transfer rate during the NO₃RR and is more conducive to the reaction. The resistance values of the EIS fitted by the three catalysts are shown in Fig. S30 (ESI†) and the inserted table. Moreover, the non-polarized cyclic voltammetry (CV) curves of these catalysts were recorded at different scan rates in the potential range of 0.75-0.85 V vs. RHE, and the ECSA was evaluated by the double layer capacitance $(C_{\rm dl})$ method (Fig. 5e and Fig. S31, ESI†). Fig. 5e shows the $C_{\rm dl}$ value calculated from the current density difference Δi at the midpoint of the measurement point interval in the CV curve and the scan rate fitting. The C_{dl} values of WO₃, Co₃O₄ and CoWO₄ are 0.099, 0.161 and 0.166 mF cm⁻¹, respectively. Obviously, CoWO₄ has the highest $C_{\rm dl}$ value, which indicates that it has the largest active surface area and more abundant active sites. Furthermore, to assess the intrinsic activities of these catalysts, we normalized the LSV curves by ECSA (Fig. 5f). In comparison, CoWO₄ continues to demonstrate the highest activity for the NO₃RR, suggesting that its enhanced catalytic performance is primarily due to the intrinsic activity of CoWO4 itself.

3.4 Catalytic mechanism analysis

To verify the catalytic process, in situ FT-IR spectroscopy was applied to identify the reaction intermediates generated during the electrocatalytic reaction and their adsorption changes. Fig. 6a-c show the in situ infrared spectra of CoWO₄, WO₃, and Co₃O₄ for the NO₃RR at different applied potentials, respectively. The initial peak observed at 1210 cm⁻¹ is indicative of the formation of *NO2 (O-N-O) intermediates. 52-54

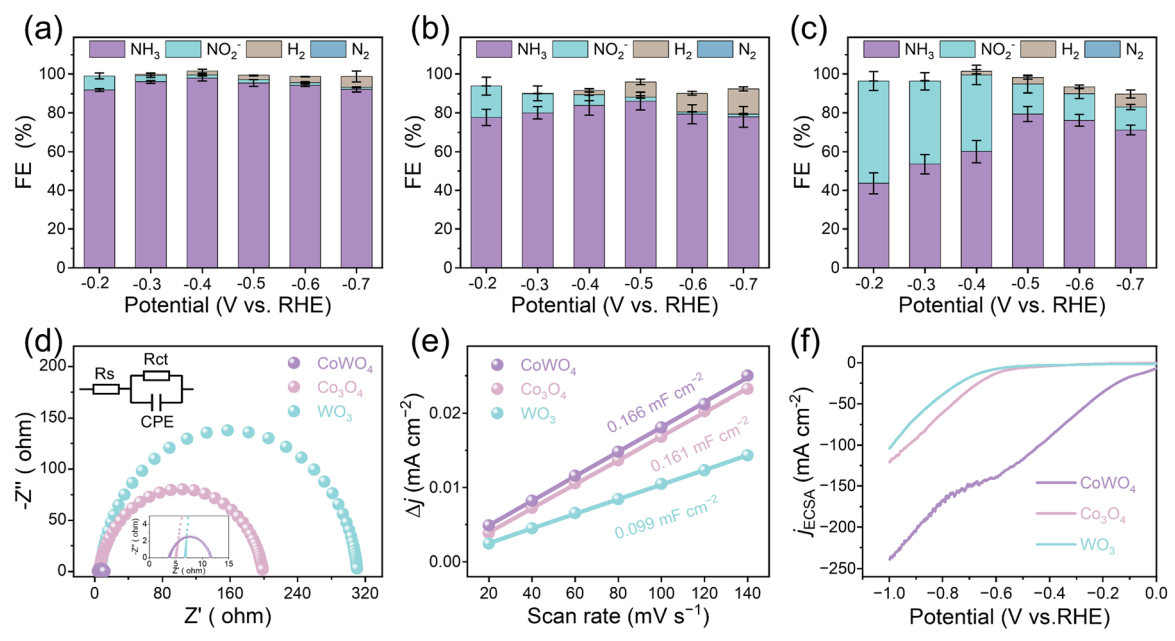


Fig. 5 (a) – (c) FEs of different products (NH $_3$, NO $_2$ $^-$, H $_2$, and N $_2$) during NO $_3$ RR electrolysis at various potentials for (a) CoWO $_4$, (b) Co $_3$ O $_4$, and (c) WO $_3$. (d) The electrochemical impedance spectra of CoWO₄, Co₃O₄, and WO₃ (the inset shows the fitted equivalent circuit model). (e) The electrochemical active surface areas. (f) LSV curves normalized by ECSA of CoWO₄, Co₃O₄, and WO₃.

Nanoscale Horizons Communication

In comparison, the vibration peak of WO₃ at 1210 cm⁻¹ exhibits a downward shift, while the vibration peaks of CoWO4 and Co₃O₄ display an upward shift. This suggests that *NO₂ can be accumulated on the surface of CoWO4 and Co3O4, while it displays a tendency of desorption onto the surface of WO₃. This result indicates that WO₃ exhibits poor adsorption of NO₂ and leads to more by-products of NO2-, while NO2- is strongly adsorbed and exhibits enhanced NO₃RR activity on the surfaces of CoWO₄ and Co₃O₄. The lower peak at 1460 cm⁻¹ and the upper peak at 1585 cm⁻¹ can be ascribed to the stretching vibration of N-H in the *NH3 intermediate, which suggests that *NH₃ is desorbed and produced NH₃ and *NH species.⁵⁵ Compared to WO₃ and Co₃O₄, these N-H vibration peaks of CoWO₄ are notably stronger, indicating the presence of significant NO₃RR processes on their surfaces. It can be clearly seen that CoWO₄ is able to enhance the hydrogenation of NO_x intermediates, which is consistent with DFT calculations. Furthermore, the downward absorption band observed near 1650 cm⁻¹ is attributed to the H-O-H bending vibration of H₂O, which reflects the dissociation of H₂O on the catalyst surface. 56 The H-O-H peak is nearly absent in WO₃, indicating its limited hydrolysis performance, which hinders hydrogenation leading to formation of the byproduct NO₂-. In comparison, the H-O-H peak in CoWO4 exhibits a low intensity

compared to Co₃O₄, demonstrating minimized hydrolytic performance, and the HER is suppressed to some extent, which contributes to its high selectivity to NH3. Consequently, a reaction mechanism for the NO₃RR over CoWO₄ catalysts was proposed (Fig. 6d). CoWO₄ not only enhances the adsorption and hydrogenation of *NO_r intermediates but also minimizes the HER, thus facilitating a highly efficient and selective NO₃RR to produce NH3.

4. Conclusions

In conclusion, CoWO₄ nanoparticles with Co-W dual sites have been developed to enhance the hydrogenation of *NOx intermediates and decrease the competitive HER to significantly enhance the NO₃RR for NH₃ production. Theoretical DFT calculations suggest that the Co sites in CoWO₄ facilitate the adsorption of NO_x intermediates, while the W sites decrease the HER. These two sites work synergistically to promote NH₃ formation. As predicted by DFT calculations, we synthesize pure phase CoWO₄ nanoparticles by a facile ion precipitation method. The electrochemical tests demonstrate that CoWO4 exhibits enhanced NO₃RR performance across a broader potential range (approximately -0.2 to -0.7 V vs. RHE), with a faradaic efficiency

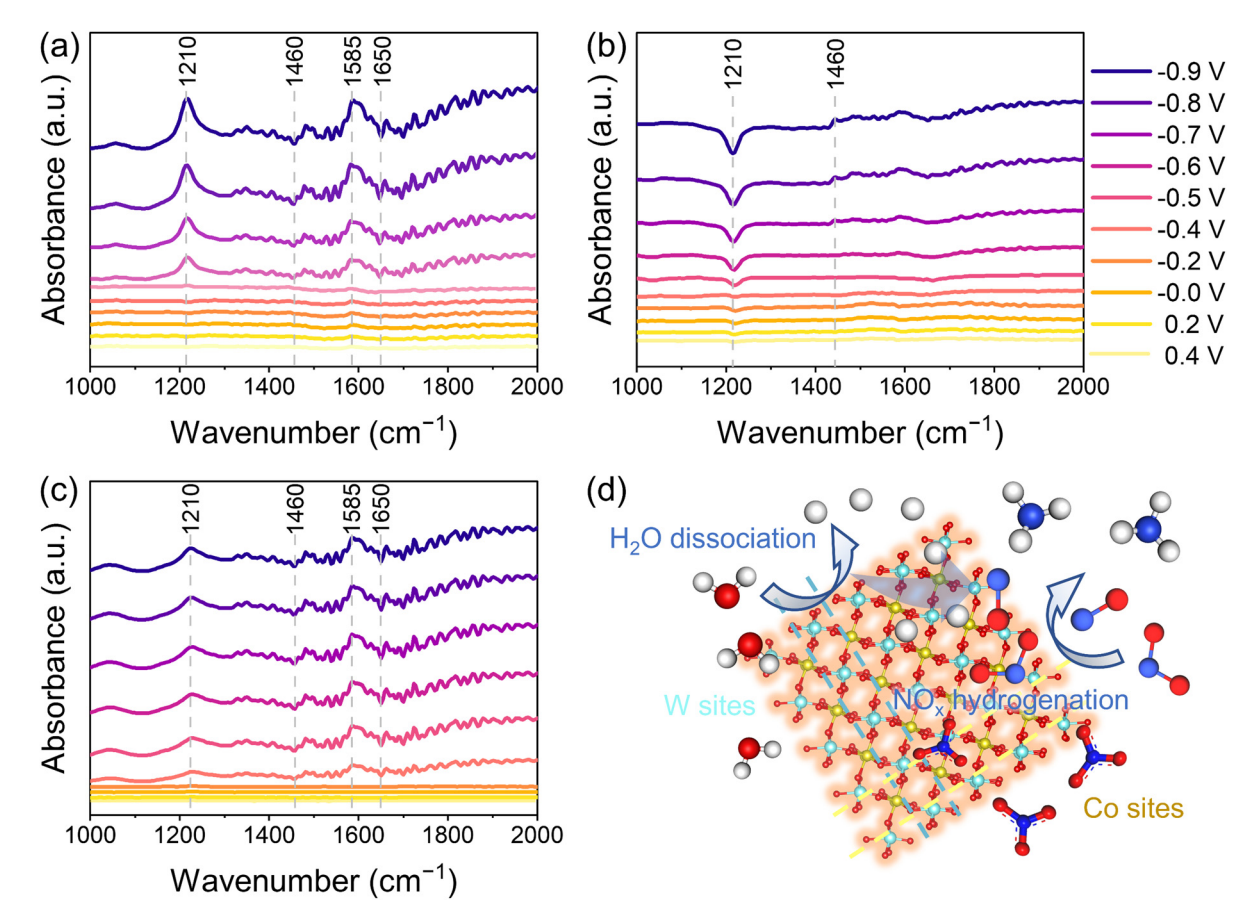


Fig. 6 In situ FT-IR spectra of (a) CoWO₄, (b) WO₃, and (c) Co₃O₄ at different applied potentials. (d) Proposed catalytic reaction mechanism for NH₃ formation on CoWO₄.

exceeding 91.7% at all test potentials, which is much higher than those of WO₃ and Co₃O₄ materials. Especially, the maximum FE of NH₃ generation on CoWO₄ is 97.8 \pm 1.5% at a potential of -0.4 V, which is significantly higher than that of WO $_{3}$ (60.1 \pm 5.8%) and Co_3O_4 (83.9 \pm 5.1%). At a potential of -0.7 V, the maximum yield of NH₃ reaches 13.2 mg h⁻¹ cm⁻². *In situ* FT-IR spectroscopy provides further evidence for the enhanced adsorption and hydrogenation behaviors of *NO_r on CoWO₄ as well as decreased HER, which aligns well with the DFT calculation

results. This study introduces a novel and efficient strategy for

designing effective NO₃RR electrocatalysts to synthesize NH₃.

Data availability

Communication

The authors declare that all data in this manuscript are available upon reasonable request.

Conflicts of interest

The authors declare no conflicts of interest.

Acknowledgements

This work received financial support from the National Natural Science Foundation of China (22072183) and the Natural Science Foundation of Hunan Province, China (2022][30690). This work was supported in part by the High Performance Computing Center of Central South University.

References

- 1 Z. Wu, Y. Song, H. Guo, F. Xie, Y. Cong, M. Kuang and J. Yang, Interdiscip. Mater., 2024, 3, 245–269.
- 2 G. Soloveichik, Nat. Catal., 2019, 2, 377-380.
- 3 K. Zhang, Y. Liu, Z. Pan, Q. Xia, X. Huo, O. C. Esan, X. Zhang and L. An, EES Catal., 2024, 2, 727-752.
- 4 G. Qing, R. Ghazfar, S. T. Jackowski, F. Habibzadeh, M. M. Ashtiani, C.-P. Chen, M. R. Smith, III and T. W. Hamann, Chem. Rev., 2020, 120, 5437-5516.
- 5 J. Ba, H. Dong, M. Odziomek, F. Lai, R. Wang, Y. Han, J. Shu, M. Antonietti, T. Liu, W. Yang and Z. Tian, Adv. Mater., 2024, 36, 2400396.
- 6 H. Zhang, K. Fang, J. Yang, H. Chen, J. Ning, H. Wang and Y. Hu, Coord. Chem. Rev., 2024, 506, 215723.
- 7 Y. Li, Z. Lu, L. Zheng, X. Yan, J. Xie, Z. Yu, S. Zhang, F. Jiang and H. Chen, Energy Environ. Sci., 2024, 17, 4582-4593.
- 8 R. Zhang, S. Zhang, H. Cui, Y. Guo, N. Li and C. Zhi, Next Energy, 2024, 4, 100125.
- 9 Z. Wu, Y. Song, Y. Liu, W. Luo, W. Li and J. Yang, Chem. Catal., 2023, 3, 100786.
- 10 L. Chen, Y. Hao, J. Chu, S. Liu, F. Bai and W. Luo, Chin. J. Catal., 2024, 58, 25-36.
- 11 L. Cai, A. Zhang, Y. Liang, X. Fan, X. He, C. Yang, L. Ouyang, D. Zheng, S. Sun, Y. Luo, Q. Liu, S. Alfaifi, A. Farouk, M. S. Hamdy, W. Zheng, Q. Kong and X. Sun, Mater. Today Energy, 2023, 38, 101428.

- 12 J. Liang, Z. Li, L. Zhang, X. He, Y. Luo, D. Zheng, Y. Wang, T. Li, H. Yan, B. Ying, S. Sun, Q. Liu, M. S. Hamdy, B. Tang and X. Sun, Chem, 2023, 9, 1768-1827.
- 13 W. Zhong, Z. Gong, P. Chen, Q. Cao, X. Liu, Y. Chen and Z. Lin, Chem. Catal., 2024, 4, 101060.
- 14 X. Fan, D. Zhao, Z. Deng, L. Zhang, J. Li, Z. Li, S. Sun, Y. Luo, D. Zheng, Y. Wang, B. Ying, J. Zhang, A. A. Alshehri, Y. Lin, C. Tang, X. Sun and Y. Zheng, Small, 2023, 19, 2208036.
- 15 D. Liu, L. Qiao, S. Peng, H. Bai, C. Liu, W. F. Ip, K. H. Lo, H. Liu, K. W. Ng, S. Wang, X. Yang and H. Pan, Adv. Funct. Mater., 2023, 33, 2303480.
- 16 Y. Xu, K. Ren, T. Ren, M. Wang, Z. Wang, X. Li, L. Wang and H. Wang, Appl. Catal., B, 2022, 306, 121094.
- 17 X. Fan, C. Liu, Z. Li, Z. Cai, L. Ouyang, Z. Li, X. He, Y. Luo, D. Zheng, S. Sun, Y. Wang, B. Ying, Q. Liu, A. Farouk, M. S. Hamdy, F. Gong, X. Sun and Y. Zheng, Small, 2023, 19, 2303424.
- 18 Y. Wei, J. Huang, H. Chen, S.-J. Zheng, R.-W. Huang, X.-Y. Dong, L.-K. Li, A. Cao, J. Cai and S.-Q. Zang, Adv. Mater., 2024, 36, 2404774.
- 19 Z. Huang, B. Yang, Y. Zhou, W. Luo, G. Chen, M. Liu, X. Liu, R. Ma and N. Zhang, ACS Nano, 2023, 17, 25091-25100.
- 20 W. Chen, X. Yang, Z. Chen, Z. Ou, J. Hu, Y. Xu, Y. Li, X. Ren, S. Ye, J. Qiu, J. Liu and Q. Zhang, Adv. Funct. Mater., 2023, 33, 2300512.
- 21 T. Zhang, M.-Y. Wu, D.-Y. Yan, J. Mao, H. Liu, W.-B. Hu, X.-W. Du, T. Ling and S.-Z. Qiao, Nano Energy, 2018, 43, 103-109.
- 22 A. Muthurasu, V. Maruthapandian and H. Y. Kim, Appl. Catal., B, 2019, 248, 202-210.
- 23 B. Wang, X. Chen, Y. He, Q. Liu, X. Zhang, Z. Luo, J. V. Kennedy, J. Li, D. Qian, J. Liu and G. I. N. Waterhouse, Appl. Catal., B, 2024, 346, 123741.
- 24 Y. Zhao, C. Chang, F. Teng, Y. Zhao, G. Chen, R. Shi, G. I. N. Waterhouse, W. Huang and T. Zhang, Adv. Energy Mater., 2017, 7, 1700005.
- 25 K. Yang, S.-H. Han, C. Cheng, C. Guo, T. Li and Y. Yu, J. Am. Chem. Soc., 2024, 146, 12976-12983.
- 26 M. Zhang, Z. Ma, S. Zhou, C. Han, V. Kundi, P. V. Kumar, L. Thomsen, B. Johannessen, L. Peng, Y. Shan, C. Tsounis, Y. Yang, J. Pan and R. Amal, ACS Catal., 2024, 14, 11231-11242.
- 27 B. Yang, Y. Zhou, Z. Huang, B. Mei, Q. Kang, G. Chen, X. Liu, Z. Jiang, M. Liu and N. Zhang, Nano Energy, 2023, 117, 108901.
- 28 J. Wang, C. Cai, Y. Wang, X. Yang, D. Wu, Y. Zhu, M. Li, M. Gu and M. Shao, ACS Catal., 2021, 11, 15135-15140.
- 29 Z. Deng, C. Ma, Z. Li, Y. Luo, L. Zhang, S. Sun, Q. Liu, J. Du, Q. Lu, B. Zheng and X. Sun, ACS Appl. Mater. Interfaces, 2022, 14, 46595-46602.
- 30 X. Wang, S. Li, Z. Yuan, Y. Sun, Z. Tang, X. Gao, H. Zhang, J. Li, S. Wang, D. Yang, J. Xie, Z. Yang and Y.-M. Yan, Angew. Chem., Int. Ed., 2023, 62, e202303794.
- 31 P. Liu, B. Wang, C. Wang, L. Ma, W. Zhang, E. Hopmann, L. Liu, A. Y. Elezzabi and H. Li, Adv. Funct. Mater., 2024, 34, 2400760.
- 32 K. Li, Y. Yin and P. Diao, Small, 2024, 20, 2402474.
- 33 Y. Tong, H. Guo, D. Liu, X. Yan, P. Su, J. Liang, S. Zhou, J. Liu, G. Q. Lu and S. X. Dou, Angew. Chem., Int. Ed., 2020, 59, 7356-7361.

34 J. Liu, C. Tang, Z. Ke, R. Chen, H. Wang, W. Li, C. Jiang, D. He, G. Wang and X. Xiao, *Adv. Energy Mater.*, 2022, 12, 2103301.

Nanoscale Horizons

- 35 Z. Shu, H. Chen, X. Liu, H. Jia, H. Yan and Y. Cai, *Adv. Funct. Mater.*, 2023, **33**, 2301493.
- 36 Y. Zhao, Y. Ding, W. Li, C. Liu, Y. Li, Z. Zhao, Y. Shan, F. Li, L. Sun and F. Li, *Nat. Commun.*, 2023, **14**, 4491.
- 37 V. P. Singh, G. Singh, R. Patel, U. K. Gaur and M. Sharma, *J. Environ. Chem. Eng.*, 2023, **11**, 111208.
- 38 C. Huang, D. Wang, W. Zhang, S. J. Yoo, X. Zhou, K. Song, Z. Chen, X. Zou, N. Yue, Z. Wang, J.-G. Kim and W. Zheng, Cell Rep. Phys. Sci., 2022, 3, 101115.
- 39 R. Nasser, H. Zhou, F. Li, H. Elhouichet and J.-M. Song, J. Colloid Interface Sci., 2024, 654, 805–818.
- 40 Z. Niu, S. Fan, X. Li and G. Chen, *Adv. Energy Mater.*, 2024, **14**, 2303515.
- 41 Z. Wang, C. Zhu, Z. Ni, H. Hojo and H. Einaga, *ACS Catal.*, 2022, **12**, 14976–14989.
- 42 D. Lu, T. Liu, J. Han, J. Zhao and H. Wang, *Chem. Eng. J.*, 2023, 477, 146896.
- 43 Y. Gao, R. Wang, Y. Li, E. Han, M. Song, Z. Yang, F. Guo, Y. He and X. Yang, *Chem. Eng. J.*, 2023, 474, 145546.
- 44 J. Zhang, J. Liu, X. Wang, J. Mai, W. Zhao, Z. Ding and Y. Fang, *Appl. Catal.*, *B*, 2019, **259**, 118063.
- 45 R. J. Colton and J. W. Rabalais, Inorg. Chem., 1976, 15, 236-238.

- 46 X. Li, G. Zhang, N. Zhang, Y. Luo, P. Shen, X. Li and K. Chu, *New J. Chem.*, 2022, **46**, 14724–14730.
- 47 D. Chen, S. Zhang, X. Bu, R. Zhang, Q. Quan, Z. Lai, W. Wang, Y. Meng, D. Yin, S. Yip, C. Liu, C. Zhi and J. C. Ho, *Nano Energy*, 2022, 98, 107338.
- 48 P. Shen, G. Wang, K. Chen, J. Kang, D. Ma and K. Chu, *J. Colloid Interface Sci.*, 2023, **629**, 563–570.
- 49 B. Li, F. Xia, Y. Liu, H. Tan, S. Gao, J. Kaelin, Y. Liu, K. Lu, T. J. Marks and Y. Cheng, *Nano Lett.*, 2023, 23, 1459–1466.
- 50 J. Ni, J. Yan, F. Li, H. Qi, Q. Xu, C. Su, L. Sun, H. Sun, J. Ding and B. Liu, *Adv. Energy Mater.*, 2024, **14**, 2400065.
- 51 Y. You, H. Chen, J. Guo, Z. Feng, J. Zhan, F. Yu and L.-H. Zhang, *Appl. Catal.*, *B*, 2025, **363**, 124837.
- 52 N. C. Kani, N. H. L. Nguyen, K. Markel, R. R. Bhawnani, B. Shindel, K. Sharma, S. Kim, V. P. Dravid, V. Berry, J. A. Gauthier and M. R. Singh, Adv. Energy Mater., 2023, 13, 2204236.
- 53 H. Sun, H. Wang and Z. Qu, ACS Catal., 2023, 13, 1077–1088.
- 54 J.-Y. Fang, Q.-Z. Zheng, Y.-Y. Lou, K.-M. Zhao, S.-N. Hu, G. Li, O. Akdim, X.-Y. Huang and S.-G. Sun, *Nat. Commun.*, 2022, 13, 7899.
- 55 Y. Zhang, H. Zheng, K. Zhou, J. Ye, K. Chu, Z. Zhou, L. Zhang and T. Liu, Adv. Mater., 2023, 35, 2209855.
- 56 J. Zhou, M. Wen, R. Huang, Q. Wu, Y. Luo, Y. Tian, G. Wei and Y. Fu, *Energy Environ. Sci.*, 2023, **16**, 2611–2620.